

Melt Electrowriting Allows Tailored Microstructural and Mechanical Design of Scaffolds to Advance Functional Human Myocardial Tissue Formation

Miguel Castilho,* Alain van Mil,* Malachy Maher, Corina H. G. Metz, Gernot Hochleitner, Jürgen Groll, Pieter A. Doevendans, Keita Ito, Joost P. G. Sluijter,* and Jos Malda*

Engineering native-like myocardial muscle, recapitulating its fibrillar organization and mechanical behavior is still a challenge. This study reports the rational design and fabrication of ultrastretchable microfiber scaffolds with controlled hexagonal microstructures via melt electrowriting (MEW). The resulting structures exhibit large biaxial deformations, up to 40% strain, and an unprecedented compliance, delivering up to 40 times more elastic energy than rudimentary MEW fiber scaffolds. Importantly, when human induced pluripotent stem cell-derived cardiomyocytes (iPSC-CM) are encapsulated in a collagen-based hydrogel and seeded on these microstructured and mechanically tailored fiber scaffolds, they show an increase in beating rate (1.5-fold), enhanced cell alignment, sarcomere content and organization as well as an increase in cardiac maturation-related marker expression (Cx43 1.8-fold, cardiac Actin 1.5-fold, SERCA2a 2.5-fold, KCNJ2 1.5-fold, and PPARGC1a 3.6-fold), indicative of enhanced iPSC-CM maturation, as compared to rudimentary fiber scaffolds. By combining these novel fiber scaffolds with clinically relevant human iPSC-CMs, a heart patch that allows further maturation of contractile myocytes for cardiac tissue engineering is generated. Moreover, the designed scaffold allows successful shape recovery after epicardial delivery on a beating porcine heart, without negative effects on the engineered construct and iPSC-CM viability.

1. Introduction

Ischemic heart disease (IHD) and heart failure (HF) remain major causes of morbidity and mortality worldwide. Both IHD and HF patients would greatly benefit from regenerative therapies, aimed at replacing the damaged myocardium with viable functional tissue. Although cell therapy for the heart is a promising approach, both preclinical and clinical trials did not show meaningful formation of new contractile myocardium.^[1] True myocardial regeneration or repair can only be achieved by the replacement of approximately one billion cardiomyocytes (CMs) that die during a myocardial infarction. Currently, induced-pluripotent stem cells (iPSCs) are the most promising candidate for the robust generation of large numbers of human cardiomyocytes in vitro, which are required for functional restoration of the failing heart. Direct transplantation of differentiated cells demonstrated some functional improvements in rodents, pigs, and non-human primates through the repopulation

Dr. M. Castilho, M. Maher, Prof. K. Ito, Prof. J. Malda
Department of Orthopedics
University Medical Center Utrecht
Utrecht University
P.O. Box 85500, 3508 GA Utrecht, the Netherlands
E-mail: M.DiasCastilho@umcutrecht.nl; j.malda@umcutrecht.nl

Dr. M. Castilho, Dr. A. van Mil, M. Maher, C. H. G. Metz, Prof. K. Ito,
Prof. J. P. G. Sluijter, Prof. J. Malda
Regenerative Medicine Center
University Medical Center Utrecht
Uppsalalaan 8, 3584 CT Utrecht, the Netherlands
E-mail: A.vanMil@umcutrecht.nl


Dr. M. Castilho, Prof. K. Ito
Orthopaedic Biomechanics
Department of Biomedical Engineering
Eindhoven University of Technology
P. O. Box 513, 5600 MB Eindhoven, the Netherlands

Dr. A. van Mil, C. H. G. Metz, Prof. P. A. Doevendans, Prof. J. P. G. Sluijter
Department of Cardiology
Experimental Cardiology Laboratory
University Medical Center Utrecht
Utrecht University
P. O. Box 85500, 3508 GA Utrecht, the Netherlands
E-mail: J.Sluijter@umcutrecht.nl

G. Hochleitner, Prof. J. Groll
Department of Functional Materials in Medicine and Dentistry
and Bavarian Polymer Institute
University of Würzburg
Pleicherwall 2, 97070 Würzburg, Germany

Prof. P. A. Doevendans
Netherlands Heart Institute
P.O. Box 19258, 3501 DG Utrecht, the Netherlands

Prof. J. Malda
Department of Equine Sciences
Faculty of Veterinary Sciences
Utrecht University
Yalelaan 112, 3584 CM Utrecht, the Netherlands

 The ORCID identification number(s) for the author(s) of this article can be found under <https://doi.org/10.1002/adfm.201803151>.

DOI: 10.1002/adfm.201803151

of the damaged myocardium with contracting cells.^[2–5] Although promising, low cell retention after injection^[6] and the immature fetal-like phenotype of iPSC-derived cardiomyocytes, leading to limited contractility and electrical instability,^[7] are hampering its clinical use. Moreover, recent research suggests that engineering 3D scaffolds with similar properties to the native myocardial extracellular matrix (ECM) offers a promising approach to support the survival of the transferred cells and to improve their maturation.^[3,8–11] Despite these insights, current fabrication technologies still fail to include topographical 3D cues of the fibrillar native ECM^[12] and biomechanical properties of the native myocardium are thus not matched.

In this study, an electrohydrodynamic printing technique, known as melt electrowriting (MEW), was used to engineer 3D fiber scaffolds.^[13–17] In this process, electrical fields are used to draw fibers of a molten polymer onto a computer-controlled collector plate. 3D constructs are then obtained by repetitive fiber-by-fiber stacking. Process and system parameters allow the fabrication of 3D structures based on the stacking of straight fibers with resulting square^[14,17] or rectangular^[15] microstructures. Recently, we have shown that MEW scaffolds with rectangular shaped microstructures and composed of a biodegradable hydroxyl-functionalized polyester can guide the growth of cardiac-derived progenitor cells and recapitulate the structural organization of native cardiac tissue.^[15] However, these constructs had limited deformability and cycle life was not compliant enough to allow for heart anisotropic contraction.

In this study, we advanced the printing design with the aim to improve the mechanical characteristics of the resulting scaffold and to stimulate seeded induced pluripotent stem cell-derived CMs (iPSC-CMs) to form human adult-like engineered myocardium. We, therefore, generated fiber scaffolds with hexagonal 3D microstructures to allow for large and anisotropic reversible deformations. Hexagonal structures are seen ubiquitously in nature, from the macroscopic structure of beehives, to the microstructure of myocardial tissue.^[10,12] Increasing attention is being given to these structures due to their distinct mechanical properties, high porosity and potential to induce formation of aligned tissues. Thus, to assess the biological potential of these fiber scaffolds, function, morphology, and maturation of iPSC-CMs seeded in the scaffolds was investigated. Finally, the potential of minimally invasive application of the cell-laden fiber scaffolds was examined using a large-animal (porcine) model.

2. Results

2.1. Melt Electrowriting of Fibrous Scaffolds with Hexagonal Microstructures

A summary of the workflow and the fabricated 3D fiber scaffolds with ordered hexagonal microstructures is shown in **Figure 1**. To fabricate these scaffolds, we investigated the effect of the collector motion and velocity profile on two types of trajectories: Straight, $S(t)$, for squared or rectangular geometry manufacturing, and angled, $A(t)$, for hexagonal-shape geometry manufacturing (**Figure 2A,D**). On the $S(t)$ trajectories, fibers collected at the speed of 4.5 mm s^{-1} demonstrated a uniform

straight morphology. This velocity is designated as critical translation speed (CTS) and matches the point where deposited fibers transform from a sinusoidal to linear morphology (**Figure 2C**). Conversely, on the $A(t)$ trajectories, the fibers that were collected at the same CTS conditions yielded an inconsistent material deposition with fiber coiling and looping at the angled segments (**Figure 2F**). Sharper corners were obtained by modulating the corner velocity, V_{corner} , using multiple trapezoidal velocity profiles (**Figure 2E**). A twofold increase in the V_{max} and consequent V_{corner} to CTS conditions led to accurate fiber depositions at both straight and corner segments (**Figure 2F**). Next, we evaluated the accuracy of fiber deposition for different internal angles (θ) of the hexagonal geometries at different side lengths (h) (**Figure 2G–J**). The hexagons with a 30° internal angle and $400 \mu\text{m}$ side lengths showed significantly higher trajectory errors ($\approx 65\%$) when compared to both 45° ($\approx 30\%$) and 60° ($\approx 10\%$) angles (**Figure 2I**). Additionally, hexagons with $400 \mu\text{m}$ side length showed higher trajectory errors than the hexagons with $800 \mu\text{m}$ side lengths. This likely occurred due to the smaller hexagons implied more collector direction changes and, therefore, a larger lag in fiber deposition. The fabrication of 3D constructs was then evaluated by assessing the ability to consistently stack multiple microfibers (**Figure 2H,J**). We observed a significant increase in the trajectory error ($\approx 10\text{--}25\%$) when increasing the number of stacked fibers from 1 to 20 layers (**Figure 2J**). However, accurate stacking of angular microfibers with 20 layers was still feasible ($\approx 400 \mu\text{m}$ scaffold thickness; **Figure 2H**). Also, we observed that smaller side lengths showed larger trajectory errors. More details about the fabrication process can be found in Video S1 in the Supporting Information.

2.2. Improved In-Plane Biaxial Tensile Properties

After successful fabrication, the in-plane tensile behavior of the hexagonal microstructured scaffolds was compared to scaffolds with rectangular microstructures. Representative tensile stress–strain curves are shown in **Figure 3A–C**. The hexagonal scaffolds were able to extend along the x -direction to $\approx 35\text{--}40\%$ before undergoing permanent deformation, compared to $2\text{--}3.5\%$ for the rectangular (**Figure 3D**). Notably, the ability of the hexagonal scaffolds to absorb and release energy when deformed in the elastic regime was $\approx 20\text{--}40$ times higher compared to rectangular scaffolds.

Both hexagonal and rectangular microstructures showed a similar stress–strain behavior when loaded in the x - and y -direction (**Figure 3A,B**). However, the magnitude of elastic limit strain and elastic strain energy was significantly lower (**Figure 3D,E**) along the y -direction. Importantly, the hexagonal scaffolds were still able to extend five to ten times more ($\epsilon_{\text{el}} \approx 10\text{--}20\%$) than the rectangular scaffolds ($\epsilon_{\text{el}} \approx 1\text{--}1.5\%$) in the y -direction. This difference in deformation between both geometries can be observed in the macroscopic images of the successive deformed microstructures (**Figure 3A,C**). It should be noted that the higher deformation of the hexagonal cells along the x -direction was observed to be accompanied by a strong contraction along the y -direction. Furthermore, the hexagonal scaffolds exhibited a lower modulus ($\approx 5\text{--}11 \text{ MPa}$ in x -direction; $1\text{--}2 \text{ MPa}$ in y -direction) than the rectangular

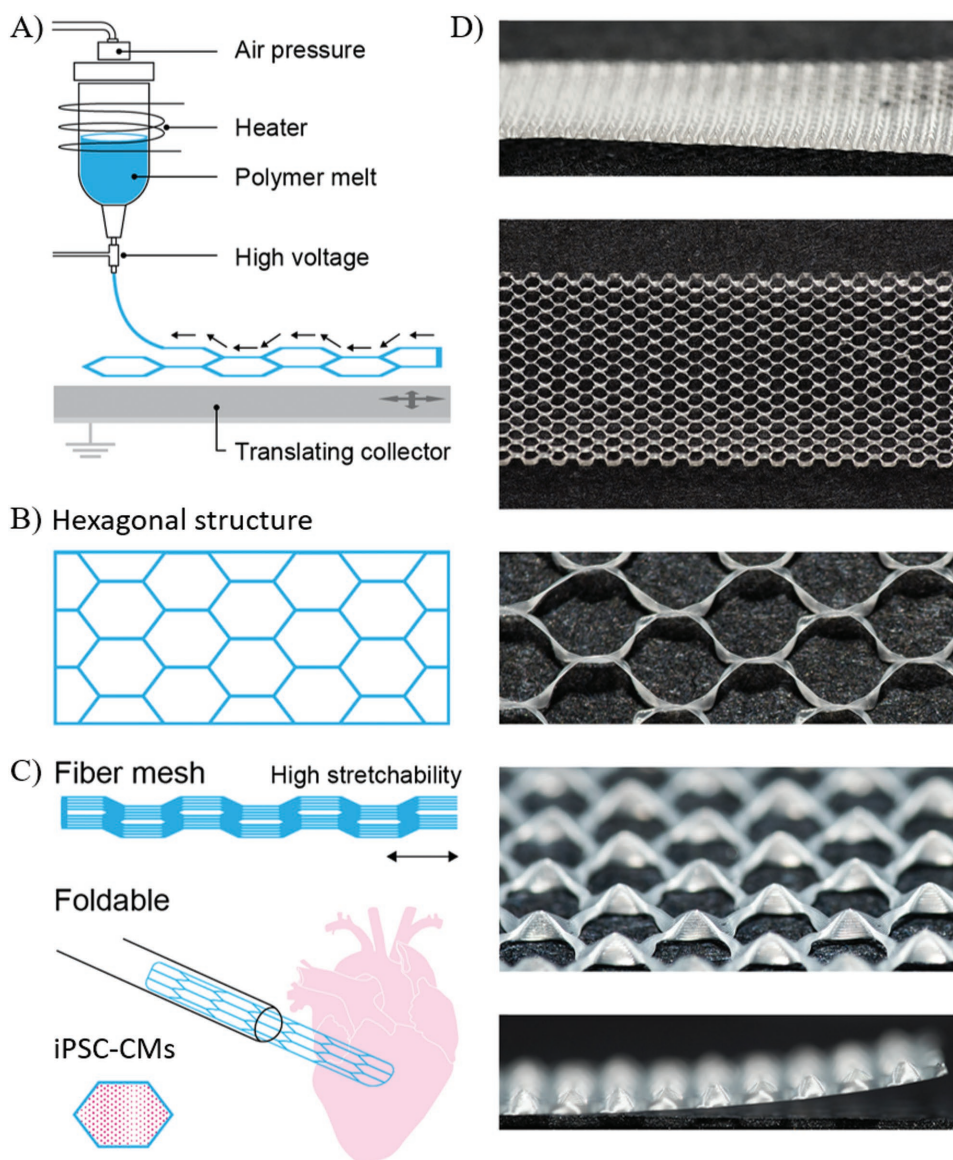


Figure 1. Representation of the workflow and fabricated microfiber scaffolds. A) Schematic illustration of the in house-built MEW device used. B) Designed hexagonal microstructure. C) 3D fiber scaffold combined with iPSC-CMs and further application in vivo through minimally invasive delivery. D) Optical images of the fabricated scaffolds: detail of microstructure with hexagonal cells (with a side length of 400 μm) composed of multiple stacked aligned microfibers. Images acquired from top and lateral perspective.

scaffolds (≈ 25 MPa in x -direction and 12 MPa in y -direction; Figure 3F). The fatigue and elastic behavior of the hexagonal microstructured scaffolds was also confirmed by evaluating their accumulated plastic strain after 50 cycles of 20% tensile strain, which was assessed to be only 0.2% (data not shown), higher than the rectangular scaffolds, depending on the hexagonal side length (Figure 3E).

2.3. Hexagonal Microstructured Scaffolds Enhance iPSC-CM Maturation

To create a functional and clinically relevant myocardial patch, fiber scaffolds (hexagonal: $\theta = 60^\circ$, $l = 400$ μm size, and

rectangular 500 $\mu\text{m} \times 1000$ μm microstructures) were subsequently combined with human iPSC-derived cardiomyocytes in a collagen-based hydrogel. The scaffold with rectangular pores of 500 $\mu\text{m} \times 1000$ μm was selected for use as a control for the 400 μm hexagonal scaffold as it has similar fiber volume fraction. The human iPSCs were differentiated into iPSC-CMs using a chemically defined, animal-free protocol.^[18] At day 7, spontaneous contractions were observed (Video S2, Supporting Information) and cardiomyocytes were subsequently purified by glucose/glutamine depletion and lactate supplementation, resulting in a $>99\%$ pure cardiomyocyte population as shown by alpha-actinin positive staining and high mitochondrial density (Figure S1, Supporting Information). iPSC-CMs were grown as monolayers and expression of sarcomeric alpha actinin, cardiac

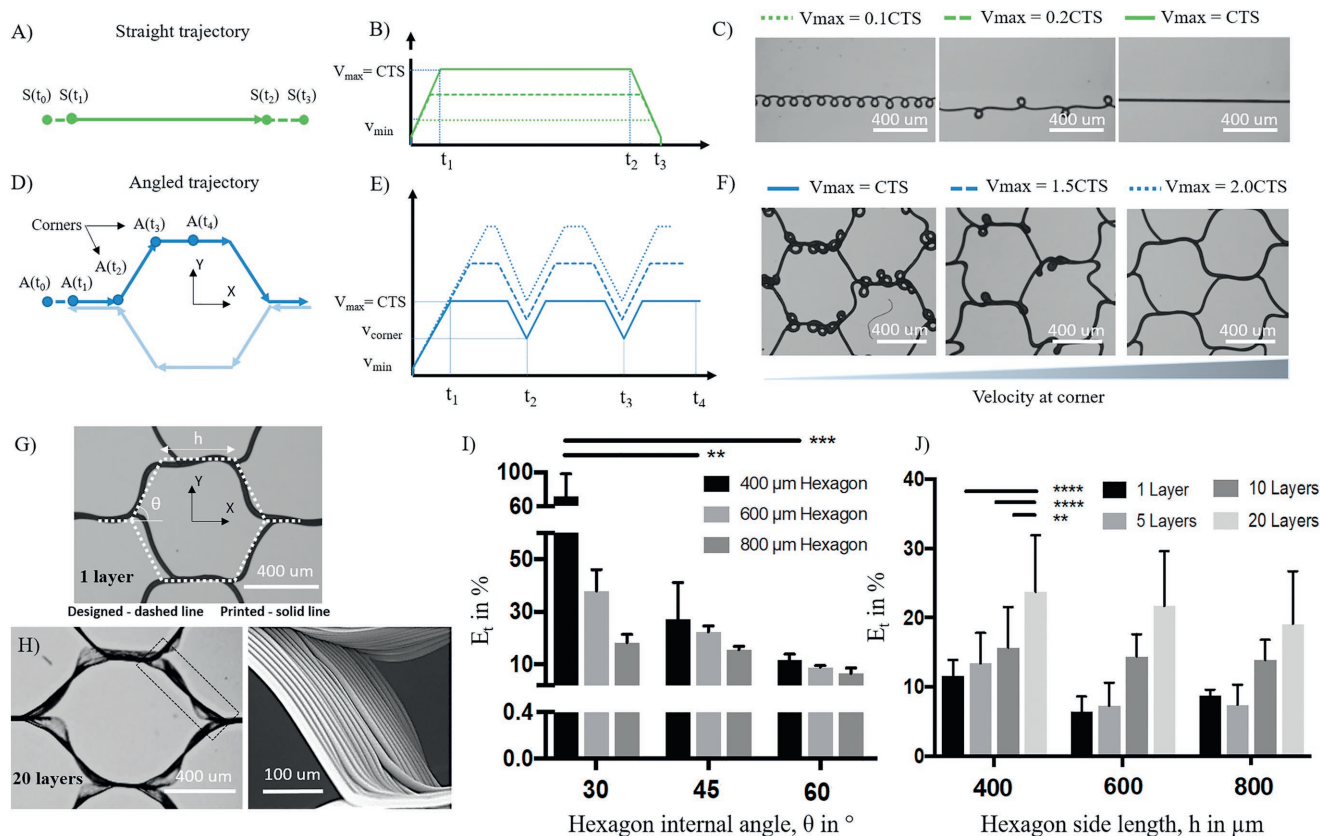


Figure 2. Fiber scaffold design and process optimization. A) trajectory of the MEW collector for straight, $S(t)$ trajectories followed by the respective B) velocity profiles and C) optical images of deposited fibers. D) trajectory of the MEW collector for angled $A(t)$ trajectories followed by the respective E) velocity profile and F) optical images of the deposited fibers. CTS, V_{\max} , V_{corner} and V_{\min} represent critical translation velocity, maximum velocity, minimum velocity, and velocity at corner, respectively. G) Designed - dashed line Printed - solid line. H) Stereoscopic (left) and scanning electron microscopy (SEM) (right) image of a hexagonal cell with a side length of $400\ \mu\text{m}$ and 20 stacked layers. Trajectory error as a function of I) internal angle and J) number of stacked layers, for different hexagonal side lengths.

troponin I, connexin 43 (Cx43) and a high mitochondrial density—characteristic for cardiomyocytes—was confirmed prior to fabrication of cardiac patches (Figure 4A–D).

To fabricate the cardiac patches, each scaffold was loaded with 1.6 million iPSC-CMs in a collagen-based hydrogel. Cell viability was assessed at day 1 showing over 90% viability of the iPSC-CMs in both rectangular and hexagonal scaffolds (Figure S2A,B, Supporting Information). Single cells were evenly distributed over the scaffolds at day 1 (Figure S2C–F, Supporting Information), and iPSC-CMs connected to form 3D structures aligned to the scaffold fibers at day 7 (Figure S2G,H, Supporting Information). At day 1, iPSC-CMs showed spontaneous contractions at the single cell level, while the iPSC-CMs began to contract synchronously across the entire scaffold at day 7 (Videos S3 and S4, Supporting Information), indicating electrophysiological coupling of the cells. Notably, the beating rate was significantly higher in the hexagonal (18.1 bpm) compared to rectangular scaffolds (12.7 bpm) (Figure 4L), showing that the mechanical properties of the scaffold allow for faster contractions.

To assess iPSC-CM organization, coupling and sarcomere density, immunofluorescent staining of the cardiac patches was performed at day 14. Staining for sarcomeric alpha-actinin

showed that the iPSC-CMs aligned to the scaffold fibers as dense 3D structures (Figure 4E,F), and sarcomere organization was present in both rectangular and hexagonal scaffolds, while hexagonal scaffolds showed enhanced sarcomere density (20x; Figure 4G,H), alignment (63x; Figure 4I,J, arrow heads), and length (Figure 4K). Connexin 43 was present throughout the cardiac patches (Figure 4G,H, arrow heads), supporting the electrophysiological coupling of the iPSC-CMs as seen after 7 d (Videos S3 and S4, Supporting Information).

In addition to sarcomere organization and Cx43 protein expression, maturation-related cardiac marker gene expression was assessed in hexagonal and rectangular scaffolds at days 7 and 14. The expression of sarcomeric (TNNI3, MYL2, MYH7), action potential-related (SCN5A, KCNJ2), electrical coupling-related (Cx43), and energy metabolism-related genes (PPARGC1a) were significantly increased at day 14 in hexagonal scaffolds compared to day 7, suggesting increased iPSC-CMs maturation over time in culture in the hexagonal scaffolds only (Figure 4M and Figure S3, Supporting Information). More importantly, the expression of alpha cardiac actin (ACTC1), mitochondrial gene (TOMM70) the calcium handling gene SERCA2a, KCNJ2, Connexin 43, and PPARGC1a were significantly increased in the hexagonal scaffolds at day 14 compared

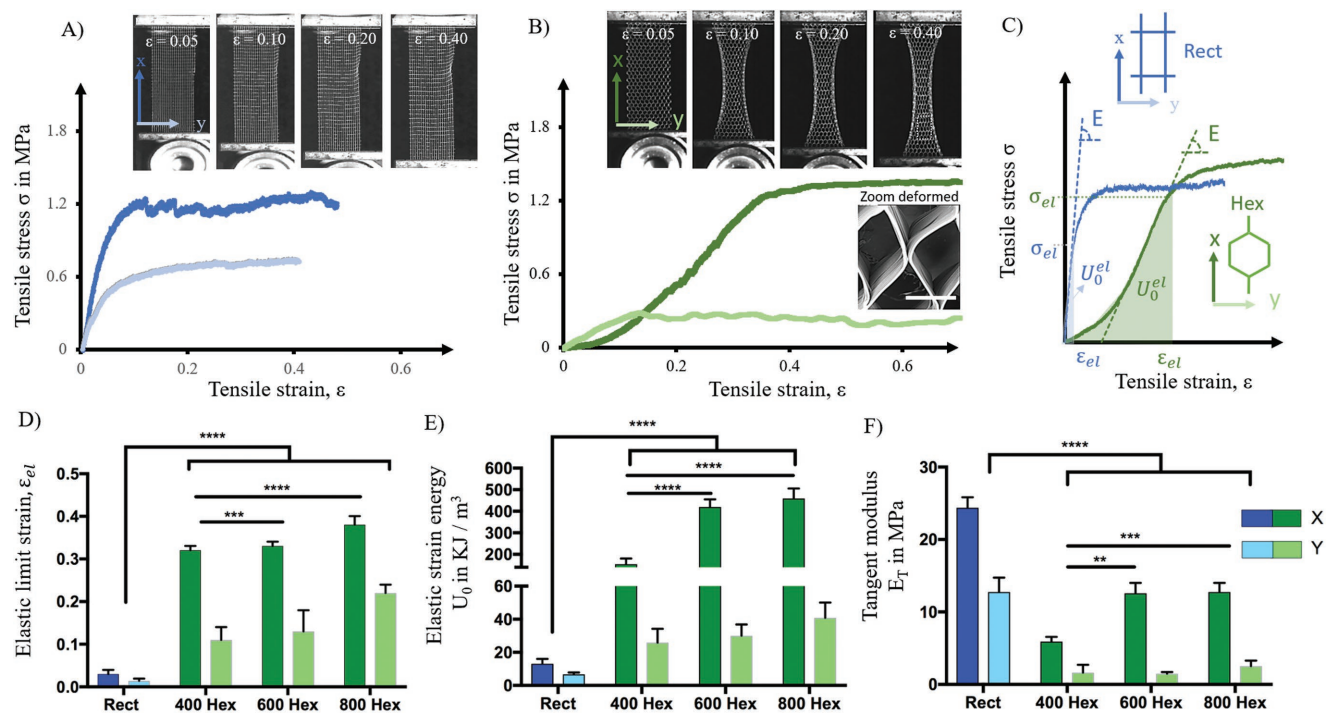


Figure 3. Mechanical behavior of the fiber scaffolds under tensile loading. Typical engineering stress–strain curves for scaffolds with A) rectangular and B) hexagonal microstructures tested in both x and y printing directions. Corresponding deformed microstructures at different strain levels for both microstructures (top row), together with a representative SEM image of the deformed hexagonal cell. C) Representation of the mechanical parameters determined from the engineering stress–strain curves, where (D) is the elastic limit strain ϵ_{el} , (E) is the elastic strain energy density, U_0^{el} , and (F) is the tangent modulus, E_T .

to the rectangular scaffolds (Figure 4M and Figure S3, Supporting Information), suggesting enhanced iPSC-CM contractile, electrical, and metabolic function, showing enhanced iPSC-CM maturation.

2.4. In Vivo Delivery of Microstructured Cardiac Patches

Cardiac patches could be applied via open-chest surgery; however, not all patients would qualify for this type of surgery and a minimally invasive approach is, therefore, preferred. To assess the feasibility of a minimally invasive delivery approach, shape recovery of cardiac patches of clinically relevant size (4 cm × 1 cm × 1 mm) (Figure 5A) was assessed after passing through a catheter-like tubing with a small inner diameter ($\varnothing = 1.5$ mm). In vitro, this revealed the quick and complete shape recovery of the patches (Figure 5B and Figure S4 and Video S5, Supporting Information). Examination of the fiber scaffold showed that its structural integrity was maintained after ejection (Figure 5C). Furthermore, we also showed the injectability and shape recovery in vivo on a beating porcine heart. A large cardiac patch, applied via the catheter-like tubing onto a beating porcine heart, evidenced shape recovery within seconds upon exposure (Figure 5D). Firm adhesion to the epicardium could be established by affixing the patch with fibrin glue. To evaluate the effect of patch delivery through the flexible tubing on cell viability, a live/dead stain was performed on injected compared to noninjected cardiac patches, showing no negative effects on iPSC-CM viability (Figure 5E–I). Moreover,

cell function was also demonstrated by evaluation of beating rate 30 min and 2 d after patch injection (Figure 5J). Spontaneous contractions were observed 30 min after passing through the tubing, followed by a significant decrease after 2 d. A similar decrease in beating rate was also observed for the noninjected patches at 2 and 5 d (Figure 4L).

3. Discussion

Elastic fiber scaffolds are a key requisite in cardiac tissue engineering for supporting and guiding contracting cells. Among the different fiber formation techniques that have been investigated, MEW is one of the most promising technologies since it enables accurate deposition of microscaled fibers. However, the high melt processing temperature, relative high applied voltage (≈ 5 kV), and lack of precise control over 3D patterning confines the material selection to thermoplastics and the layering to straight fibers, which restricts large deformations and fatigue properties of the MEW scaffolds.^[16,17,19,20] Here, we successfully 3D patterned nonlinear microfibers with ordered hexagonal microstructures. This approach demands no design of new biomaterials with improved bulk elastic properties but required an accurate modulation of the motion and velocity profile of the translating collector. Due to direction changes of the collector trajectory, an overaccumulation of drawn material at angled fiber corners was observed, which translated into inaccurate fiber stacking. This overaccumulation occurred because the collector plate decelerates before, and immediately accelerates

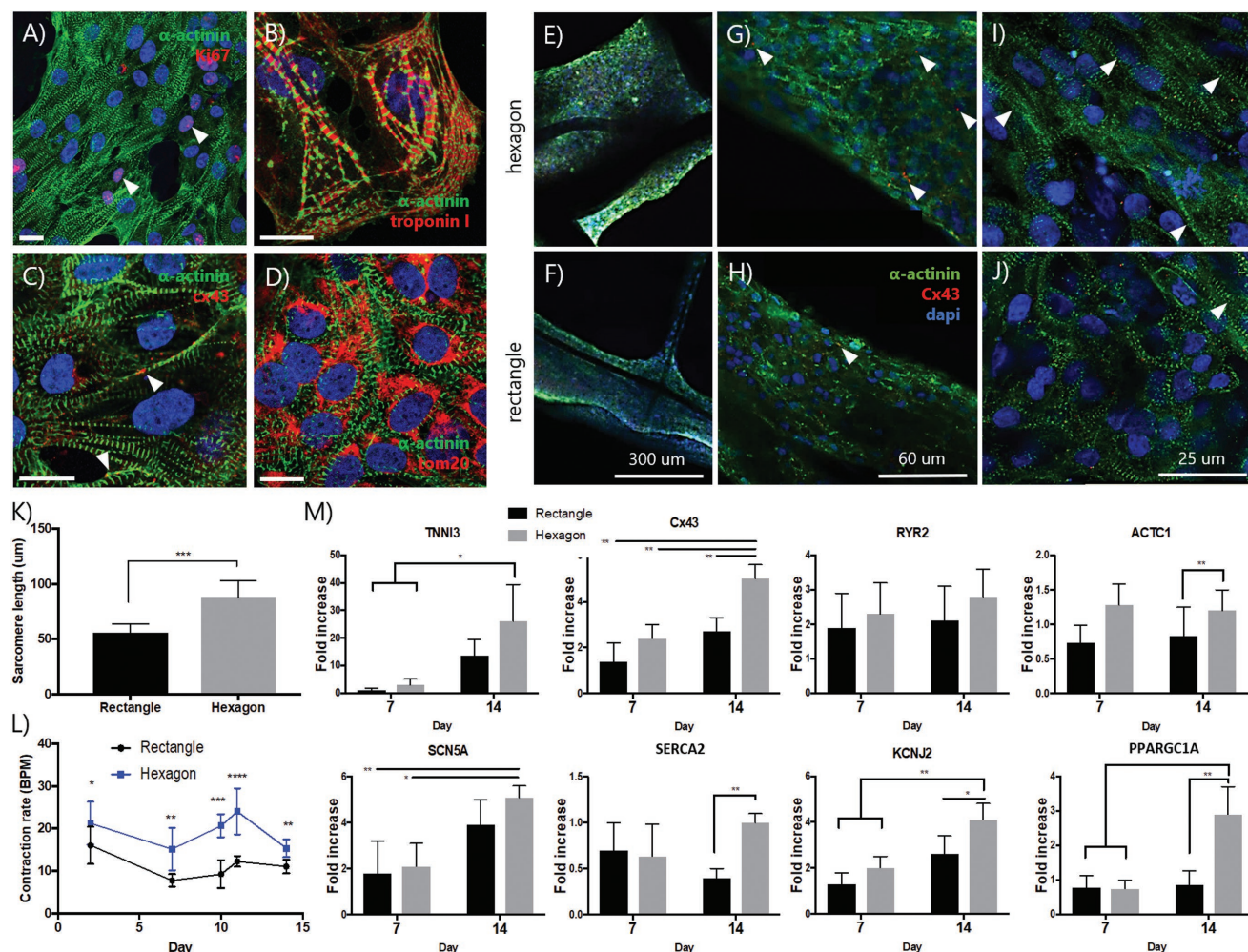


Figure 4. Hexagonal scaffolds induce iPSC-CM contractile properties and maturation. iPSC-CM characterization before combination with scaffold, showing A) proliferating cells, B) sarcomeric structures, C) Connexin 43 (Cx43), and D) mitochondrial localization. iPSC-CMs localize to both E) hexagonal and F) rectangular fiber scaffolds, and confocal microscopy shows G,H) Cx43 expression, and increased sarcomere density, I,J) alignment, and K) length in hexagonal scaffolds compared to rectangular scaffolds. L) Beating rate at days 2, 7, 10, 11, and 14. M) Cardiac marker and maturation-related gene expression in hexagonal and rectangular scaffolds at day 7 and day 14.

after the corners, thus lowering the collection conditions below the CTS. By modulating the corner velocity, we ensured that the magnitude of the velocity vector just before and after the corner were also at CTS conditions, thus preventing fiber coiling. As presented, larger angles, such as 60° , and bigger hexagonal side lengths, as $800\ \mu\text{m}$, resulted in fibers with sharper cornering, due to enhanced mechanical stretching and consequent reduction of lag in the fiber deposition. Moreover, inaccurate fiber deposition was found to occur above $\approx 400\ \mu\text{m}$, which we attributed to dielectric interference between the ejected and drawn fiber. The effect of other instrument parameters, i.e., acceleration voltage, working distance, flow rate, and applied temperature, on direct writing of fibers with a controlled angular morphology was also investigated but revealed only a minor effect, when compared with collector velocity and trajectory path.

We attribute the unprecedented in-plane biaxial deformation of our fiber scaffolds to the rationally designed scaffold microstructure. The well-organized and open cell hexagonal geometry allowed for impressive structural compliance without

requiring deformation of the fiber's bulk material. Therefore, by printing thin fibers in such unique hexagonal microstructures, we were able to create highly stretchable structures using a rather stiff thermoplastic material with very limited deformability. Such compliance is a key property for artificial muscle engineering and can be further tuned by adjusting the hexagon cell size. However, we observed that deformation and fatigue was significantly inferior along the y -direction. This is because the interfiber connectivity at the cell contact points was low, as fibers were only partially entangled. Moreover, it should be noted that the obtained tangent moduli were higher than that reported for the native cardiac tissue, i.e., $10\text{--}20\ \text{kPa}$ at early diastole and $200\text{--}500\ \text{kPa}$ at late diastole,^[21] but this can be modulated by reducing the fiber volume fraction and diameter. Other research groups have also attempted to overcome the limited stretchability of thermoplastic fiber scaffolds by manufacturing coiled fibers.^[22,23] However, biaxial patterning of coiled fibers was limited, hampering the control over their anisotropic mechanical properties. Moreover, it is also important

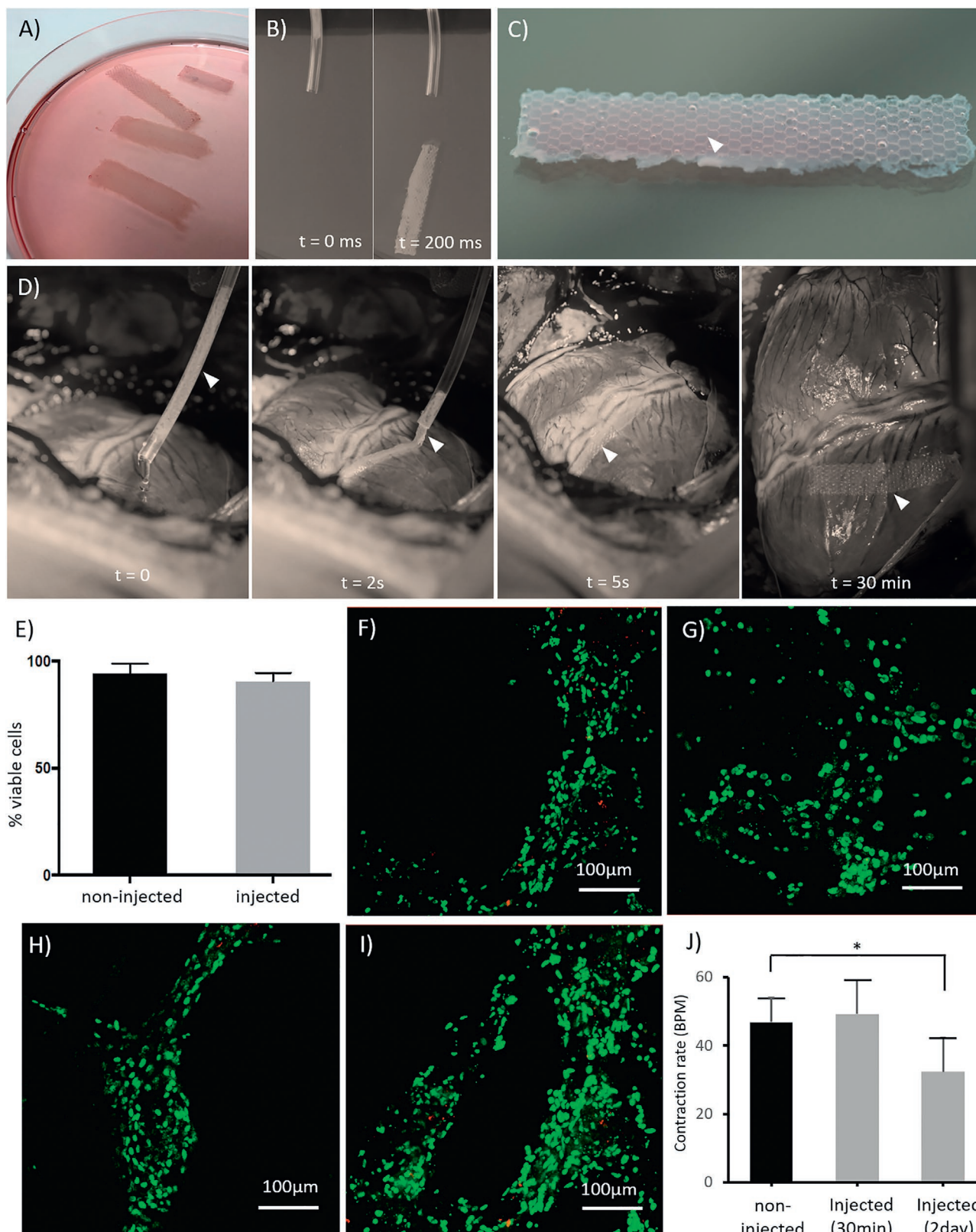


Figure 5. Injectability and in vivo placement of cardiac patch with hexagonal geometry. A) In vitro culture of cardiac patch consisting of iPSC-CMs in cardiac-like ECM on large hexagonal scaffolds. B) In vitro injectability, shape recovery, and C) macro image of cardiac patch after injection. D) Application and shape recovery of cardiac patch on beating porcine heart. E) Cell viability of in vitro F,G) noninjected and H,I) injected cardiac patches. J) Spontaneous beating rate of in vitro noninjected and injected cardiac patches 30 min and 2 d after injection.

to be mentioned that the in-plane tensile properties of the composites were dominated by the MEW fibers and that the contribution of the collagen gel was negligible, as revealed by our preliminary results on MEW fiber-collagen gel composites (data not shown). For this reason, the reported tensile tests were conducted solely on the MEW fiber scaffolds, i.e., without collagen gel.

To generate functional cardiac patches that recapitulate the endogenous myocardium, a seeding density of $\approx 80\,000$ iPSC-CMs mm^3 was used, indicating the high number of iPSC-CMs needed to fabricate the clinically relevant sized patches. The differentiation protocol used, generated beating iPSC-CMs with well-developed sarcomeres, and presence of connexin 43 ensuring cellular coupling. However, sarcomere organization and presence of some proliferation demonstrates that the cells are still at an immature stage, which is well known for iPSC-CMs at this stage of differentiation.^[24] To ensure only iPSC-CMs were seeded in the scaffolds, an iPSC-CM purification step was incorporated yielding near 100% iPSC-CMs. Although other studies have shown that the addition of fibroblasts was necessary to ensure 3D tissue formation in hydrogels,^[25] here the presence of the scaffold fibers was sufficient to induce the formation of stable tissue-like structures. In addition, the scaffolds induced the iPSC-CMs to form electrically coupled 3D structures that were aligned along the fibers after 7 d. This shows that the fiber scaffold directs iPSC-CM organization and induces the formation of an integrated patch structure, which is essential to provide contractile support in vivo. Our results also showed that remodeling and stabilization occurred in vitro, evidencing that biological patch characteristics can be tuned in vitro before application in vivo. Although both scaffold designs supported cardiac patch formation, the hexagonal scaffold patches showed several characteristics of iPSC-CM maturation after 14 d in culture; 1) enhanced structural organization concomitant with increased sarcomeric gene expression, 2) increased action potential, cell-coupling and calcium handling-related gene expression with enhanced rhythmic beating rate, and 3) increased expression of PGC1 α , the main driver of mitochondrial biogenesis and fatty acid oxidation. These data suggest that the superior compliance of the hexagonal scaffolds enhance the contractile properties of the iPSC-CMs, which is in agreement with a previous report using elastic and stiff gels.^[26] Moreover, the successfully printed hexagonal microstructures represent well the native honeycomb-like microstructure of the native myocardial tissue, formed by collagen fibers and other ECM proteins, together with embedded aligned cardiomyocytes.^[27] Despite this similarity, the honeycomb pores seen within the myocardial tissue are much more elongated and significantly smaller ($\approx 20\text{--}40\ \mu\text{m}$) than the printed hexagons ($\approx 400\text{--}800\ \mu\text{m}$), which is still a limitation of the MEW technology.

The presented potential for minimally invasive delivery opens up the great possibility of MEW constructs being delivered, e.g., during a coronary artery bypass surgery (CABG), where small incisions are needed for the surgery, and therefore large catheters ($>26\text{G}$) can be used. However, our in vivo data are solely a proof-of-principle in a porcine model with only short follow-up time efficacy evaluation in a limited number of animals. This represents not only a limitation of the current work

but also an opportunity for future investigations necessary to further develop our cardiac patches for clinical application. Subsequently, applying human iPSC-CM cells in the xeno-model of the porcine has potential limitations on an immune-rejection level that also require further investigation.

4. Conclusion

In summary, we have demonstrated, for the first time, the melt electrowriting of fiber scaffolds with well-ordered hexagonal microstructures. These scaffolds exhibited a remarkable biaxial deformation and were more suitable for supporting contracting human iPSC-CMs, driving their maturation, and support high tensile strains when placed on a contracting heart, than the conventional, nonstretchable melt written scaffolds. Taken together, we engineered clinically relevant and functional human myocardial patches with unparalleled properties for cardiac repair. In addition to cardiac tissue formation, engineering of other soft tissues can also benefit from this novel method for mechanically tailored fiber scaffold design.

5. Experimental Section

Melt Electrowriting Printing: A in-house built MEW printer was used as described in ref. [15]. Granular medical grade polycaprolactone, mPCL (Purasorb PC 12, Purac Biomaterials, Netherlands) was molten at $[85, 90]^\circ\text{C}$ in a glass syringe connected to a sealed hose delivering pressurized N_2 . The molten polymer was electrified using a high voltage source (Heinzinger, LNC 10000-5 POS, 0–10 kV) and the electrified jets were collected onto a grounded collector plate (x - y plane) controlled via an advanced 2-axis stepper motor controller (PMX-2EX-SA, ARCUS Technology Inc., USA). Trapezoidal velocity profiles were used to model both trajectories, i.e., straight, $S(t)$ and angled, $A(t)$, where t represents collection time. $S(t)$ fibers arrays ($\varnothing \approx 20\ \mu\text{m}$) were collected at $V_{\text{max}} = 4.5\ \text{mm s}^{-1}$ (defined as CTS velocity), acceleration voltage of $U_{\text{acc}} = 4.5\ \text{kV}$, collection distance of $d = 3.5\ \text{mm}$, and feeding pressure of $p = 1\ \text{bar}$, where $A(t)$ fiber arrays ($\varnothing \approx 20\ \mu\text{m}$) were manufactured with increased collector velocities $V_{\text{max}} = 1.5\ \text{CTS}$ and $V_{\text{max}} = 2.0\ \text{CTS}$, and same remaining MEW settings, i.e., $U_{\text{acc}} = 4.5\ \text{kV}$, $d = 3.5\ \text{mm}$ and $p = 1\ \text{bar}$.

In order to evaluate the fiber deposition accuracy, different hexagonal architectures with sides lengths (h) of 400, 600, and 800 μm and internal angles (θ) of 30° , 45° , and 60° were manufactured. The distance between the target shape and printed was obtained by quantifying the mean trajectory error (E_t)

$$E_t = \frac{1}{n} \sum_{i=0}^n \sqrt{(x(i) - x_t(i))^2 + (y(i) - y_t(i))^2} \quad (1)$$

where $n = 20$ is the number of data points considered. Additionally, the fiber staking precision was also investigated by determining the trajectory error for printed hexagons with 1, 5, 10, and 20 layers. A minimum of five fiber arrays was evaluated for each experiment. For subsequent mechanical and cell experiments studies fiber scaffolds ($5 \times 5\ \text{cm}^2$) having rectangular ($500\ \mu\text{m} \times 1000\ \mu\text{m}$) and hexagonal microstructure ($h = 400, 600, 800\ \mu\text{m}$ and $\theta = 60^\circ$) were manufactured at a height of $\approx 300\ \mu\text{m}$, which comprised 15 layers.

Image Analysis: Fiber arrays were examined immediately after printing using a stereo microscope (Olympus SZ61, resolution 2040×1536 pixels). Both fiber morphology and deposition trajectory were analyzed using *Image J* software. Scaffold microstructures were visualized using an SEM Phenom Pro (Phenom-World, the Netherlands) at an acceleration

voltage of 5–10 kV. Prior imaging, circular sections ($\varnothing \approx 5$ mm) were cut from each scaffold microstructure, i.e., rectangular and hexagonal, and gold plated (1 nm) using a Q150R rotary-pumped sputter (Quorum Technologies, UK).

Mechanical Analysis: Uniaxial tensile tests were performed on a universal testing machine (Zwick Z010, Germany) with a 1 kN load cell. Tests were performed at a rate of 1 mm min^{-1} at room temperature. Rectangular strips ($25 \text{ mm} \times 5 \text{ mm}$) of both hexagonal and rectangular scaffold microstructure were tested according to the x - and y -direction of the printing plane. An optical measurement system (Zwick VideoXtens multicamera, Germany) was used to monitor the corresponding microstructure deformation. At least five samples for each type and testing direction was tested. Mechanical parameters were determined from the engineering stress–strain curves namely, elastic limit stress (σ_{el}) and strain (ϵ_{el}); tangent modulus (E_T), determined by using a least square fit of the initial slope of the stress–strain elastic region as depicted in Figure 3a; and the elastic strain energy density (U_0^{el}) obtained by

$$U_0^{el} = \int_0^{\epsilon_{el}} \sigma \, d\epsilon \quad (2)$$

Furthermore, scaffolds were cyclic stretched (50x) in both directions at 10% and 20% strain.

Human iPSC Culture and Differentiation: Healthy human fibroblast-derived iPSC lines were kindly provided by the department of Cell Biology of the University Medical Center Utrecht. iPSCs were cultured in E8 medium (Thermo Fisher Scientific) on 1:400 growth-factor-reduced Matrigel (Corning). Cells were nonenzymatically passaged in a splitting ratio of 1:15–1:25 routinely at 80% confluence using $0.5 \times 10^{-3} \text{ M}$ EDTA (Thermo Fisher Scientific) every 4–5 d and E8 medium was replaced every day except the day after passaging. All pluripotent cultures were routinely tested for mycoplasma contamination using a MycoAlert Kit (Lonza). iPSCs were cultured for at least three passages before initiating cardiac differentiation and cells were used between passage 40 and 58. To obtain iPSC-derived cardiomyocytes, iPSCs were grown to maximum 85% confluence and after washing with phosphate-buffered saline (PBS), medium was changed to RPMI1640 (Gibco) supplemented with recombinant human albumin (Sigma) and ascorbic acid 2-phosphate (Sigma) (CDM3). At day 0, the medium was supplemented with $5 \times 10^{-6} \text{ M}$ CHIR99021 (Selleck Chemicals), which was replaced with CDM3 containing $2 \times 10^{-6} \text{ M}$ Wnt-C59 (Tocris Bioscience) after 48 h. Subsequently, medium changes were performed every other day, and spontaneously contracting cells were observed from days 6 to 7. To purify iPSC-CMs, CDM3 was replaced with CDM3 without D-glucose and with sodium DL-lactate (ChemCruz) for 4 d.

iPSC-CM Loading of Fiber Scaffolds: Scaffolds discs with a \varnothing of 8 mm and height of 300 μm of both hexagonal and rectangular pores were obtained from scaffold strips using a biopsy punch and sterilized using UV radiation for 30 min. After purification, iPSC-CMs were detached from their plates using 1X TrypLE Express (Thermo Fisher Scientific) and filtered through 100 μm pore filters. A total of 1.6 million iPSC-CMs in 40 μL of hydrogel, consisting of 1 mg mL^{-1} RatCol Rat Tail Type I Collagen with Neutralization Solution for 3D Gels (Advanced Biomatrix), and 1% Geltrex Matrix (Thermo Fisher Scientific) in Dulbecco's modified Eagle's medium (DMEM) (Gibco), were used for each fiber scaffold. Half of the volume (gel with cells) was casted in Teflon moulds, scaffolds were placed on top and the other half was casted on top and incubated for 45 min at 37 $^{\circ}\text{C}$ to ensure proper gelation. The patches were subsequently maintained up to 14 d in DMEM supplemented with 10% Knock-Out Serum Replacement (Thermo Fisher Scientific) and 2% B27 (Thermo Fisher Scientific).

Cell Viability: Cell viability in the constructs was assessed at days 1 and 7 by using a LIVE/DEAD Viability/Cytotoxicity Kit (Thermo Fisher Scientific). Calcein AM was used to produce an intense uniform green fluorescence in live cells, while ethidium homodimer-1 was used to produce a bright red fluorescence in dead cells (Thermo Fisher, L3224). The constructs were imaged using a Leica SP8X confocal microscope and the number of live and dead cells was quantified using ImageJ.

Quantitative Real-Time Polymerase Chain Reaction (qRT-PCR) Analysis: Total RNA was isolated with TriPure Isolation Reagent (Roche Applied Science) and treated with RNase-free DNase I (Qiagen). 500 ng of total, DNA-free, RNA was transcribed to cDNA using the iScript cDNA Synthesis Kit (Bio-Rad), and qRT-PCR was performed using iQ SYBR Green Supermix (Bio-Rad) and specific primers in a CFX96 Touch Real-Time PCR detection system (Bio-Rad). Used qRT-PCR conditions were: 5 min at 95 $^{\circ}\text{C}$, followed by 40 cycles of 15 s at 95 $^{\circ}\text{C}$, 30 s at specific annealing temperature, and 45 s at 72 $^{\circ}\text{C}$, followed by melting curve analysis to confirm single product amplification. Messenger RNA expression levels were normalized to β -actin mRNA expression (ΔCt), and relative differences were calculated ($\Delta\Delta\text{Ct}$) and presented as fold induction ($2^{\Delta\Delta\text{Ct}}$). All measurements were performed in duplo. Primers used are shown in the Supplementary Information.

Immunofluorescent Staining: At days 7 and 14 the patches were fixed using 4% paraformaldehyde (PFA) at room temperature for 15 min. After washing with Dulbecco's phosphate-buffered saline (DPBS), patches were permeabilized using 0.1% Triton-X-100 (Sigma-Aldrich) at room temperature for 10 min and blocked in 10% goat serum (Sigma-Aldrich) at room temperature for 30 min. Next, primary antibodies against sarcomeric alpha actinin (Sigma, A7811, 1:200) and Connexin 43 (Thermo Fisher Scientific, 71-0700, 1:200) were added and incubated DPBS at 4 $^{\circ}\text{C}$ overnight. Patches were washed with PBS and incubated with Goat antimouse Alexa fluor-488, and Goat antirabbit Alexa fluor-555 secondary antibodies (Thermo Fisher Scientific, 1:500), and 1 $\mu\text{g mL}^{-1}$ Hoechst (Thermo Fisher Scientific) in DPBS in the dark at room temperature for 4 h. Images were captured using the Leica SP8X confocal microscope and sarcomere quantifications were performed using ImageJ.

In Vivo Cardiac Patch Delivery: All animal experiments were approved by the Ethical Committee on Animal Experimentation of the University Medical Center Utrecht (Utrecht, the Netherlands) and conform to the "Guide for the care and use of laboratory animals". Pretreatment, anesthesia, intubation, mechanical ventilation, opening of the thorax, and maintenance anesthesia protocols have been described in detail in ref. [28]. Animals ($n = 2$) were kept fasted the day of surgery and animals were immunosuppressed by Cyclosporin A (CsA) one day before patch placement. Animals were sacrificed by exsanguination under general anesthesia.

Statistical Analysis: Multiple T-tests were used to compare the means of multiple groups, and two-way Anova's were used to compare the results of the hexagonal and rectangles. Differences were considered significant at a probability of error (p) of $p < 0.05$. All data were completed with at least three samples per group.

Supporting Information

Supporting Information is available from the Wiley Online Library or from the author.

Acknowledgements

M.C., A.v.M., J.P.G.S. and J.M. contributed equally to this work. The authors gratefully thank the following agencies for their financial support: the strategic alliance University Medical Center Utrecht – Technical University Eindhoven, the European Research Council (ERC) (consolidator grants 3D-JOINT (#647426), Evicare (#725229), and Design-2Heal (#617989)), the Technobeat (668724), the Project SMARTCARE-II of the Biomedical Materials Institute, cofunded by the ZonMw-TAS program (#116002016), the Dutch Ministry of Economic Affairs, Agriculture and Innovation and the Netherlands CardioVascular Research Initiative (CVON): the Dutch Heart Foundation, Dutch Federations of University Medical Centers, the Netherlands Organization for Health Research and Development, and the Royal Netherlands Academy of Sciences. The authors would like to thank A. K. Braat in the Department of Cell Biology, University Medical Center

Utrecht for providing iPSC lines and R. G. C. Maas, J. H. van Duijn, and M. Ainsworth for technical assistance with culturing of iPSCs and scaffold fabrication. The corresponding authors of this manuscript were updated on October 4, 2018, following initial online publication.

Conflict of Interest

The authors declare no conflict of interest.

Keywords

bioinspired materials, cardiac tissue engineering, induced pluripotent stem cells, melt electrowriting, stretchable fiber scaffolds

Received: May 7, 2018

Revised: July 9, 2018

Published online: August 13, 2018

- [1] R. Madonna, L. Van Laake, S. Davidson, F. Engel, D. Hausenloy, S. Lecour, J. Lecor, C. Perrino, R. Schulz, K. Landmesser, C. Mummery, S. Janssens, J. Willerson, T. Eschenhagen, P. Ferdinandy, J. Sluijter, *Eur. Heart J.* **2016**, *14*, 1789.
- [2] Y. Shiba, T. Gomibuchi, T. Seto, Y. Wada, H. Ichimura, Y. Tanaka, T. Ogasawara, K. Okada, N. Shiba, K. Sakamoto, D. Ido, T. Shiina, M. Ohkura, J. Nakai, N. Uno, Y. Kazuki, M. Oshimura, I. Minami, U. Ikeda, *Nature* **2016**, *538*, 388.
- [3] L. Ye, Y. Chang, Q. Xiong, P. Zhang, L. Zhang, P. Somasundaram, M. Lepley, C. Swingen, L. Su, J. Wendel, J. Guo, A. Jang, D. Rosenbush, L. Greder, J. Dutton, J. Zhang, T. Kamp, D. Kaufman, Y. Ge, J. Zhang, *J. Zhang, Cell Stem Cell* **2014**, *15*, 750.
- [4] J. Riegler, M. Tiburcy, A. Ebert, E. Tzatzalos, U. Raaz, O. Abilez, Q. Shen, N. Kooreman, E. Neofytou, V. Chen, M. Wang, T. Meyer, P. Tsao, A. Connolly, L. Couture, J. Gold, W. Zimmermann, *J. Wu Circ. Res.* **2015**, *117*, 720.
- [5] J. Chong, X. Yang, C. Don, E. Minami, Y. Liu, J. Weyers, W. Mahoney, B. Biber, S. Cook, N. Palpant, J. Gantz, J. Fugate, V. Muskheili, G. Gough, K. Vogel, C. Astley, C. Hotchkiss, A. Baldessari, L. Pabon, H. Reinecke, E. Gill, V. Nelson, H. Kiem, M. Laflamme, C. Murry, *Nature* **2014**, *510*, 273.
- [6] F. van den Akker, D. Feyen, P. van den Hoogen, L. van Laake, E. van Eeuwijk, I. Hoefler, G. Pasterkamp, S. Chamuleau, P. Grundeman, P. Doevendans, P. Sluijter, *Eur. Heart J.* **2016**, *38*, 184.
- [7] C. Veerman, G. Kosmidis, C. Mummery, S. Casini, A. Verkerk, M. Bellin, *Stem Cells Dev.* **2015**, *24*, 9.
- [8] Q. Wang, H. Yang, A. Bai, W. Jiang, X. Li, X. Wang, Y. Mao, C. Lu, R. Qian, F. Guo, T. Ding, H. Chen, S. Chen, J. Zhang, C. Liu, N. Sun, *Biomaterials* **2016**, *105*, 52.
- [9] L. Gao, M. Kupfer, J. Jung, L. Yang, P. Zhang, Y. Sie, Q. Tran, V. Ajeti, B. Freeman, V. Fast, P. Campagnola, B. Ogle, J. Zhang, *Circ. Res.* **2017**, *120*, 1318.
- [10] G. Engelmayr, M. Cheng, C. Bettinger, J. Borenstein, R. Langer, L. Freed, *Nat. Mater.* **2008**, *7*, 1003.
- [11] M. Montgomery, S. Ahadian, L. Huyer, M. Rito, R. Civitarese, R. Vanderlaan, J. Wu, L. Reis, A. Momen, S. Akbari, A. Pahnke, R. Li, C. Calderone, M. Radisic, *Nat. Mater.* **2017**, *16*, 1038.
- [12] K. Weber, *J. Am. Coll. Cardiol.* **1989**, *13*, 1637.
- [13] T. Brown, P. D. Dalton, D. Huttmacher, *Adv. Mater.* **2011**, *23*, 5651.
- [14] G. Hochleitner, T. Jüngst, T. Brown, K. Hahn, C. Moseke, F. Jakob, P. Dalton, J. Groll, *Biofabrication* **2015**, *7*, 035002.
- [15] M. Castilho, D. Feyen, M. Flandes-Iparraguirre, G. Hochleitner, J. Groll, P. Doevendans, T. Vermonden, K. Ito, J. Sluijter, J. Malda, *Adv. Healthcare Mater.* **2017**, *6*, 1700311.
- [16] M. de Ruijter, A. Hrynevich, J. Haigh, G. Hochleitner, M. Castilho, J. Groll, J. Malda, P. D. Dalton, *Small* **2018**, *14*, 1702773.
- [17] F. Wunner, M. Wille, T. G. Noonan, O. Bas, P. D. Dalton, E. M. De-Juan-Pardo, D. W. Huttmacher, *Adv. Mater.* **2018**, *30*, 1706570.
- [18] P. Burrridge, E. Matsa, P. Shukla, Z. Lin, J. Churko, A. Ebert, F. Lan, S. Diecke, B. Huber, N. Mordwinkin, J. Plews, O. Abilez, B. Cui, J. Gold, J. Wu, *Nat. Methods* **2014**, *11*, 855.
- [19] M. Castilho, G. Hochleitner, W. Wilson, B. van Rietbergen, P. D. Dalton, J. Groll, J. Malda, K. Ito, *Sci. Rep.* **2018**, *8*, 1245.
- [20] A. Hrynevich, B. S. Elçi, J. N. Haigh, R. McMaster, A. Youssef, C. Blum, T. Blunk, G. Hochleitner, J. Groll, P. D. Dalton, *Small* **2018**, *14*, 1800232.
- [21] K. Nakano, M. Sugawara, K. Ishihara, S. Kanazawa, W. Corin, S. Denslow, R. Biederman, B. Carabello, *Circulation* **1990**, *82*, 1352.
- [22] S. Fleischer, R. Feiner, A. Shapira, J. Ji, X. Sui, H. Wagner, T. Dvir, *Biomaterials* **2013**, *34*, 8599.
- [23] O. Bas, D. Angella, J. Baldwin, N. Castro, F. Wunner, N. Saidy, S. Kollmannsberger, A. Reali, E. Rank, E. De-Juan-Pardo, D. Huttmacher, *ACS Appl. Mater. Interfaces* **2017**, *9*, 29430.
- [24] V. Christiaan, K. Georgios, M. Christine, C. Simona, V. Arie, B. Milena, *Stem Cells Dev.* **2015**, *24*, 1035.
- [25] B. Liao, C. Jackman, Y. Li, N. Bursac, *Sci. Rep.* **2017**, *7*, 42290.
- [26] A. Engler, C. Carag-Krieger, C. Johnson, M. Raab, H. Tang, D. Speicher, J. Sanger, J. Sanger, D. Discher, *J. Cell Sci.* **2008**, *121*, 3794.
- [27] G. Macchiarelli, O. Ohtani, S. A. Nottola, T. Stallone, A. Camboni, I. Prado, P. Motta, *Histol. Histopathol.* **2002**, *17*, 699.
- [28] S. Koudstaal, S. Jansen of Lorkeers, J. Ghoe, G. van Hout, M. Jansen, P. Gründeman, G. Pasterkamp, P. Doevendans, I. Hoefler, S. Chamuleau, *J. Visualized Exp.* **2014**, *86*, 51269.